Progress in Additive Manufacturing
https://doi.org/10.1007/s40964-023-00543-3

FULL RESEARCH ARTICLE

Dimensionless quantities in discrete element method: powder model parameterization for additive manufacturing

Simon Girnth[1] · Tim Heitkamp[1] · Christian Wacker[2] · Nils Waldt[1] · Günter Klawitter[1] · Klaus Dröder[2]

Received: 7 June 2023 / Accepted: 17 November 2023

Abstract
Powder bed-based additive manufacturing processes offer an extended freedom in design and enable the processing of metals, ceramics, and polymers with a high level of relative density. The latter is a prevalent measure of process and component quality, which depends on various input variables. A key point in this context is the condition of powder beds. To enhance comprehension of their particle-level formation and facilitate process optimization, simulations based on the Discrete Element Method are increasingly employed in research. To generate qualitatively as well as quantitatively reliable simulation results, an adaptation of the contact model parameterization is necessary. However, current adaptation methods often require the implementation of models that significantly increase computational effort, therefore limiting their applicability. To counteract this obstacle, a sophisticated formula-based adaptation and evaluation method is presented in this research. Additionally, the developed method enables accelerated parameter determination with limited experimental effort. Thus, it represents an integrative component, which supports further research efforts based on the Discrete Element Method by significantly reducing the parameterization effort. The universal nature of deducting this method also allows its adaptation to similar parameterization problems and its implementation in other fields of research.

Keywords Discrete element method · DEM · Powder bed · Additive manufacturing · Pi-theorem · Dimensionless numbers

1 Introduction

Additive manufacturing has revolutionized the engineering landscape, offering unprecedented opportunities for increased customization, improved material efficiency, and the ability to produce complex geometries. One type of methods in this category can be summarized as powder bed-based techniques. Particularly laser powder bed fusion (LPBF) offers specific advantages such as excellent spatial resolution, high part density, and compatibility with a wide range of materials. Despite its significant potential, the process optimization of LPBF remains a key challenge, particularly due to the complex interrelations of various influencing quantities and interacting physical effects [1, 2]. A critical aspect of this challenge lies in the study of powder-related phenomena, as the handling of powders and their solidification are essential in-processing procedures during powder bed-based additive manufacturing [3]. With the intention of optimizing the resulting component of quality, the goal of process development is to characterize any correlations. This enables a predictability of the process results as well as a targeted choice of process parameter values for optimal results.

✉ Simon Girnth
simon.girnth@hs-hannover.de

Tim Heitkamp
tim.heitkamp@hs-hannover.de

Christian Wacker
c.wacker@tu-braunschweig.de

Nils Waldt
nils.waldt@hs-hannover.de

Günter Klawitter
guenter.klawitter@hs-hannover.de

Klaus Dröder
k.droeder@tu-braunschweig.de

[1] Faculty II, Hochschule Hannover, University of Applied Sciences and Arts, 30459 Hannover, Germany

[2] Institute for Machine Tools and Production Technology, Technische Universität Braunschweig, 38106 Braunschweig, Germany

Published online: 26 January 2024

To identify possible relationships, process virtualization by means of computational approaches has recently become a focus of research. Compared to physical approaches, analyses based on virtual process models do not tend to introduce interfering influences, as it offers the possibility to exclude them during modeling and to precisely define input variables independently. Furthermore, virtual approaches allow easier access to state and process variables in a wide range of the spatial size scale. However, there is a conceptual and parametric modeling effort, which arises in the formulation and evaluation of the simulation model.

In the context of in-processing, the objects of investigation are typically associated with the scales of average sized components (macroscopic scale, $> 10^{-3}$ m), melt pools (mesoscopic scale, $\approx 10^{-5}$ to 10^{-3} m) and microscopic structures of the material (microscopic scale, $< 10^{-5}$ m) [4, 5]. Essential goal for examinations of the mesoscopic scale is to gain insight into the physical interactions within the powder volume. A widespread tool for this is the implementation of simulations utilizing the Discrete Element Method (DEM), which allows for a mapping of the kinetic interaction of discrete particles among other physical interactions. The implementation of DEM is specifically advantageous for inquiries yielding results directly from characteristics of powder grains, such as grain size distribution, grain shape, and mechanical properties, especially applicable when geometric restrictions prevent consideration as a continuum. Within these constraints, DEM enables an analysis of mechanisms that govern powder deposition in powder bed additive manufacturing, since typical layer thicknesses range from about 20 to 100 µm and are, therefore, comparable in size to typical grain diameters [6–11].

To derive reliable statements from the results of simulations, both the adaptation and the validation of the model parameterization are required, which up to now often have been associated with extensive experimental effort [6, 12–15]. To mitigate this, an adaptation and validation method is presented in the following chapters. By combining the results of few physical reference experiments with a dimensionless correlation of bulk density, angle of repose and input variables of DEM simulations, the method derived in the research presented here enables a formula-based parameterization of the powder model.

2 Discrete Element Method

To characterize phenomena related to particle dynamics in powder bed additive manufacturing, the prevailing approach is to use DEM models composed of problem-specific subsidiary models. In the following sections, relevant models are introduced to examine the interrelationships inherent in the parameterization of the composite model. The fundamental equations and models of DEM are then elucidated to illustrate the underlying correlations, resulting possibilities, and requirements related to simulation parameterization. Subsequently, the need for further reduction of both computational and experimental effort is highlighted by discussing current strategies in the literature to reduce simulation and parameter optimization effort.

2.1 Governing Equations and Subsidiary Models

The basic conceptual model of DEM is based on Newton's second law of motion and can be used to describe interactions between a variety of discrete bodies, which differ in their properties. The governing equilibrium conditions for DEM are obtained for particle i and its contact partners j as force and torque equilibriums for three translational and rotational degrees of freedom, respectively. Thus, it holds

$$(m\ddot{s})_i = m_i g + \sum_j F_n^{ij} + F_{nd}^{ij} + F_t^{ij} + F_{td}^{ij} + F_{ko}^{ij}, \tag{1}$$

$$(I\dot{\omega})_i = \sum_j M_r^{ij} + \left(F_t^{ij} + F_{td}^{ij}\right) \times r_k^{ij}, \tag{2}$$

where g is the acceleration due to gravity, $\ddot{s}_\mathrm{i}$ is the translational acceleration, $\dot{\omega}_\mathrm{i}$ is the rotational acceleration, I_i is the moment of inertia, m_i is the mass of the i-th powder grain and F_n^{ij} is the normal force in the direction of the grain radius resulting from the interaction with contact partner j. F_t^{ij} and F_{ko}^{ij} are, with analogous indexing, the tangential force and the cohesive force. The rotational degrees of freedom are represented by the rotation angle vector ω_i, with M_r^{ij} as the torque due to rolling friction and r^{ij} as the effective contact radius, which depicts the distance between the centers of the contacting particles and their point of contact.

Accounting to the more spherical grain shape of powder particles commonly used in powder bed-based additive manufacturing, DEM contact forces can be calculated based on the overlap depth δ of two bodies in spherical contact. The applicability of corresponding models can be distinguished, for example, according to cohesion and compressibility, which models the plastic deformability of the powder. Since AM powders can be classified as incompressible and conditionally cohesive [16], elastic-adhesive models are particularly suitable for describing the contacts. These models in turn consist of subsidiary models for the representation of the contact force in the radial direction (e.g., the Hertzian contact model [17], extended by an adhesion model such as suggested by Johnson et al. [18] for elastically deformable particles) and tangential direction (such as Mindlin [19]) in addition with damping forces in the same directions (such as Tsui et al. [20]).

The Hertzian contact model [17] describes the contact force as an elastic spring force of two bodies in contact due to a deformation at the contact point. For a contact of two spherical bodies, the contact force perpendicular to the surface is given by

$$F_{nH}^{ij} = 4/3 \cdot E^{ij} \cdot \left(r^{ij}\right)^{-1} \cdot \left(a^{ij}\right)^{3}, \tag{3}$$

with

$$E^{ij} = E_i \cdot E_j \cdot \left[E_j \cdot \left(1 - \nu_i^2\right) \cdot E_i \cdot \left(1 - \nu_j^2\right)\right]^{-1}, \tag{4}$$

$$r^{ij} = r_i \cdot r_j \cdot \left(r_i + r_j\right)^{-1}, \tag{5}$$

$$a^{ij} = \left(r^{ij} \cdot \delta_n^{ij}\right)^{0.5}, \tag{6}$$

where r_i, r_j describe the radii of the contact partners. The radius of the flattened circular surface at the contact point is described by a^{ij}, where δ_n^{ij} describes the overlap depth of the contact partners in the normal direction. E^{ij} describes the effective Young's modulus, E_i, E_j the respective Young's moduli and ν_i, ν_j the Poissons's ratios of the contact partners. Substituting Eqs. 5 and 6 into Eq. 3 yields

$$F_{nH}^{ij} = 4/3 \cdot E^{ij} \cdot \left(r^{ij}\right)^{0.5} \cdot \delta_n^{ij1.5}. \tag{7}$$

With stiffness in normal direction

$$k_n^{ij} = 4/3 \cdot E^{ij} \cdot a^{ij}, \tag{8}$$

Eq. 7 yields

$$F_{nH}^{ij} = k_n^{ij} \cdot \delta_n^{ij}. \tag{9}$$

According to Tsuji et al. [20], a dissipative component can be considered in the same direction with the definition of a viscous damping term. In this case, the damping force F_{nd} scales with the coefficient of restitution c_{res}, which can be formulated as a quotient of the velocities before and after impact. It holds

$$F_{ndTTI}^{ij} = -2 \cdot \sqrt{5/6} \cdot \ln\left(c_{res}\right) \cdot \left(\ln^2\left(c_{res}\right) + \pi^2\right)^{-0.5} \cdot \left(k_n^{ij} \cdot m^{ij}\right)^{0.5} \cdot \dot{\delta}_n^{ij}, \tag{10}$$

with

$$c_{\mathrm{res}} = v_{c1}/v_{c2}, \tag{11}$$

where $\dot{\delta}_{\mathrm{n}}^{\mathrm{ij}}$ is the relative velocity of the collision partners in the normal direction. The effective mass m^{ij} is considered analogously to r^{ij} and E^{ij}, with

$$m^{ij} = m_i \cdot m_j \cdot \left(m_i + m_j\right)^{-1}. \tag{12}$$

Similar to the Hertzian contact model, the contact models according to Mindlin [19] also describe a contact force as an ideal elastic spring force of two bodies in contact. The following applies to the tangential force according to Mindlin

$$F_{tM}^{ij} = k_t^{ij} \cdot \delta_t^{ij}, \tag{13}$$

with the displacement tangential to the sphere radius at the contact point $\delta_{\mathrm{t}}^{\mathrm{ij}}$ and the tangential stiffness

$$k_t^{ij} = 8 \cdot G^{ij} \cdot a^{ij}, \tag{14}$$

where the effective shear modulus G^{ij} is formulated analogously to E^{ij} (Eq. 4). The relationship

$$G = E/2(1 + \nu), \tag{15}$$

eliminates the shear modulus as a parameter to be considered in the adaptation of the material model. With the implementation of macroslip as Coulomb's friction [21], the following applies for the tangential force

$$F_t^{ij} = \begin{cases} F_{tM}^{ij}; & \left|F_t^{ij}\right| \le \mu_s^{ij} \cdot \left|F_n^{ij}\right| \\ \mu_s^{ij} \cdot \left|F_n^{ij}\right| \cdot \left(F_t^{ij} / \left|F_t^{ij}\right|\right); & \text{else} \end{cases}. \tag{16}$$

The dissipative part in tangential direction F_{td}^{ij} is considered analogous to the normal direction by implementing the tangential stiffness with

$$F_{tdTTI}^{ij} = -2 \cdot \sqrt{5/6} \cdot \ln\left(c_{\mathrm{res}}\right) \cdot \left(\ln^2\left(c_{\mathrm{res}}\right) + \pi^2\right)^{-0.5} \cdot \left(k_t^{ij} \cdot m^{ij}\right)^{0.5} \cdot \dot{\delta}_t^{ij}. \tag{17}$$

Adhesion between powder particles can occur due to capillary forces (caused by moisture), Coulomb forces (caused by electrostatic charge) and van der Waals forces. As AM powders typically contain a low moisture content, the capillary force density is correspondingly low. With respect to force density, the same applies to electrostatic forces in electrically conducting materials [22–24] or material pairings, which have similar electron affinities and therefore triboelectrically charge to a negligible extent. To compare the force densities of adhesion effects, not only the number of relevant contacts but also the relative force effect per contact must be considered. In a typical AM powder particle size range (10–100 µm), the forces differ by about + 200% (capillary force) and – 95% (force due to electrostatic charge) from the centrally located van der Waals force [25–28]. This suggests, that adhesion forces in dry AM powders are dominated by van der Waals forces. For modeling van der Waals forces in DEM, the model according to Johnson et al. [18] has been used in recent literature [6, 9, 29–31]. This model correlates the surface energy density w_{JKR} with the

contact force according to the Hertzian model, to infer the resulting normal force as

$$F_{nJKR}^{ij} = 4/3 \cdot E^{ij} \cdot \left(r^{ij}\right)^{-1} \cdot a^{ij3} - \left(16 \cdot \pi \cdot w_{\mathrm{JKR}} \cdot E^{ij} \cdot a^{ij3}\right)^{0.5}. \tag{18}$$

The first term of the right-side equals F_{nH}^{ij} (Eq. 7) with repulsive character, the second term expresses the counteracting adhesive force F_{ad}^{ij}. Equation 18 gives the critical values for the size of the contact area as well as for the overlap (Eq. 6) and thus for the tensile force where the contact pair detaches [32, 33], described as

$$F_{\mathrm{JKR\ krit}}^{ij} = -3/2 \cdot \pi \cdot w_{\mathrm{JKR}} \cdot r^{ij}. \tag{19}$$

For evaluation of the torque equilibrium and the resulting angular acceleration, the modeling of the torque due to rolling friction M_r^{ij} is necessary. In this context, the rolling friction value μ_r is used to compensate for a flawed representation of grain shape [34, 35]. This can result from the approximation of non-spherical grain shapes with monospherical bodies, which are applied due to modeling simplicity rather than more accurate representations by polyspherical bodies. According to a computationally efficient model, M_r^{ij} can be considered as proportional to the angular velocity of the i-th particle $\dot{\omega}_i$ [34, 36] by

$$M_{r1}^{ij} = -\mu_r \cdot \left|F_n^{ij}\right| \cdot r^{ij} \cdot \dot{\omega}_i. \tag{20}$$

More plausible from a physical point of view, but also more computationally intensive, is a consideration based on the mean angular velocity $\dot{\omega}_{\mathrm{ij}}$ of the contact pair [34, 37] with

$$M_{r2}^{ij} = -\mu_r \cdot \left|F_n^{ij}\right| \cdot r^{ij} \cdot \dot{\omega}_{ij}. \tag{21}$$

In comparison, the first model meets the requirements of considering high particle counts the most, which is a relevant factor when performing powder bed simulations.

Common Approaches for Simulation Effort Reduction and Parameterization.

According to the previously listed equations, input variables of the force and torque equilibrium (Eqs. 1, 2) result to $E, \nu, \rho, r, c_{\mathrm{res}}, \mu_s, \mu_r$ and w_{JKR}. Their numerical adaptation is carried out in a compromise between the optimization of computation time and resulting simulation accuracy. Regarding the computation time optimization in DEM, it is prevalent to lower the Young's moduli E_{real} to E_{sim} (index *sim* denotes quantities, that are used in the virtual environment), which is reduced by several orders of magnitude compared to the physical reality (denoted by index *real*) [11, 14, 38]. This results in longer contact times, which in turn allows for larger time steps and thus a reduction of the computational effort. In addition to the dynamics of the simulated problem, the degree of reduction especially depends on the preservation of similarity within the model parameterization [14]. Regarding the similarities when scaling E_{sim}, equilibrium condition terms are proportional to E_{sim} for F_n^{ij}, F_t^{ij} and M_r^{ij}, while F_{nd}^{ij}, F_{td}^{ij} and F_{ko}^{ij} are proportional to $E_{\mathrm{sim}}^{0,5}$. With the common reduction of $E_{\mathrm{sim}} = 2/3 \cdot E_{\mathrm{real}}$ [38–40], e.g., from 10^9 to 10^6 Pa for metallic materials, a skewness of about 20% between the terms may result, which could influence the simulation result.

Another approach to mitigate the computational effort is to reduce the number of particles or to increase the particle radius [41]. Besides reducing the number of calculated contacts per volume, this approach also enables an increase of the time step T_{r} [42–45] in accordance with the linear relation

$$T_{\mathrm{r}} = \left(\pi \cdot r_{\mathrm{min}} \cdot (\rho/G)^{0.5}\right)/(0.163 \cdot \nu + 0.8766). \tag{22}$$

However, this procedure is only possible if the aspect ratio between particles and geometry elements investigated in the simulation is sufficiently large and entails an adjustment of the relation of body and surface forces [38] according to

$$F_{\mathrm{JKR\ krit}}^{ii}/F_g^i \sim w_{\mathrm{JKR}} \cdot r^{ii}/\left(r^{i3} \cdot g\right). \tag{23}$$

Here, F_g^i corresponds to an inertial force due to the acceleration by gravity g and results for a spherical body to

$$F_g^i = \rho \cdot 0.75 \cdot \pi \cdot r^{i3} \cdot g. \tag{24}$$

Thus, if the radius of the particles is doubled, w_{JKR} must be quadrupled according to the proportionality in Eq. 23. In addition to literature given parameters (E, ν, ρ), adaptation parameters commonly used in the context of parametrization and validation of DEM models for AM powders are friction values $\mu_{\mathrm{s}}, \mu_{\mathrm{r}}$, the coefficient of restitution c_{res} and the surface energy density w_{JKR}. In this respect, literature-based adaptation methods range from physical measurement of grain-specific quantities [13, 35, 46, 47], to iterative simulative approximation of physically determined macroscopic values [6, 13–15, 47–50], pragmatic parameterization based on literature values [46, 51] and finally to the adaptation in one distinct parameter [38]. In the latter, the surface energy density is particularly well suited as an adaptation parameter for grain sizes typical of AM powders due to a comparatively high sensitivity [16, 38]. Oriented to the stress state and dynamics during powder application, the validity of the model parameterizations is often referred to macroscopic reference values, such as the angle of repose α_{s} and/or the bulk density ρ_{s} [6, 12–14, 46, 49, 52, 53]. Thus, the prevailing methodology can be generalized as a partial parameter determination via physical experiments supplemented with literature values,

combined with a simplified statistical approach for adjusting the remaining parameters based on macroscopic quantities. Applicability is limited mainly by the use of simplistic statistical methods, which require a significant number of virtual experiments and associated computational effort, and by the reduced validity of parameterizations when using pre-adapted values from different sources. Therefore, a standardized methodology that implements a sophisticated, resource-efficient approach needs to be explored.

3 Methods and Materials

The following sections assume a contact model composed of several sub-models, including Hertz and Mindlin's normal and tangential forces, damping forces in corresponding directions as suggested by Tsuji et al., an adhesive force element derived from Johnson et al. studies, and a standard rolling friction model. Thus, for a contact pair of defined materials, at least four adaptation parameters are available (c_{res}, μ_s, μ_r and w_{JKR}). If all these parameters are adapted simulatively, a considerable computational effort is required, especially when investigating multiple materials. Moreover, the results thus derived lack unequivocal validity.

To counteract these drawbacks, an adaptation method (Fig. 1) is presented below, in which the number of unknown parameters is initially reduced through physical experiments. Further parameter selection is based on dimensionless quantities Π correlating the model parameters, the angle of repose and the bulk density. In addition, the derivation and determination of the dimensionless quantities is also performed in this research.

To provide for a targeted adaptation of the selected model parameters, the parameterizations of the performed simulations are systematically scattered around expected values. In this respect, $w_{\mathrm{JKR\,sim}}$ is initialized by ranges of values commonly found in literature [6, 9, 29–31], while $\mu_{\mathrm{r\,sim}}$ is motivated by deviations in grain morphology of monospherical bodies used in simulation and the result of physical determinations [34, 35]. Hence, data on grain size distributions and grain shapes are first determined experimentally. Afterwards, the determined values are supplemented by coefficients of sliding friction $\mu_{\mathrm{s\,real}}$, coefficients of restitution $c_{\mathrm{res\,real}}$, angles of repose $\alpha_{\mathrm{s\,real}}$ and bulk densities $\rho_{\mathrm{s\,real}}$, which are also determined experimentally. The corresponding methods are presented in the following chapters. To evaluate the applicability of the method on different classes of material encountered in powder bed-based additive manufacturing, this study conducts investigations on AlSi10Mg (type: AlSi10Mg.02; distributor: m4p material solutions GmbH, Magdeburg-Germany), Al_2O_3 (type: BAK40; distributor: xtra GmbH, Leonberg-Germany) and Polyether ether ketone (PEEK; type: Vestakeep 2000 FP; distributor: Evonik AG, Essen-Germany).

3.1 Physical Characterization Methods

To reduce the number of parameters to be adapted simulatively and to correlate with physical reference experiments, $\mu_{\mathrm{s\,real}}$, $c_{\mathrm{res\,real}}$, $\alpha_{\mathrm{s\,real}}$, $\rho_{\mathrm{s\,real}}$, and grain size distribution data are determined in this study according to the physical experimental methods presented below. Standard deviations are given as expanded standard deviations according to ISO/IEC Guide 98–3:2008–09 method A [54].

Determination of Particle Morphology The description of particle morphology consists of a qualitative description of the sphericity and roundness of particles of the investigated AM powders studied, as well as the particle size distribution and corresponding distribution values. Roundness refers to the ratio between the mean radii of curvature of the convex regions of a particle and the radius of its enveloping circle. The sphericity of a particle indicates the ratio between the circumference of an equal-area circle and the actual circumference. Both values refer to two-dimensional projections. The evaluation of the grain shape is based on SEM images of the investigated powders (Fig. 2, analyzed with a Supra 55VP, Gemini; manufacturer: Carl Zeiss AG, Jena-Germany).

The grains of the AlSi10Mg powder are less round due to bonded satellites and have a lower sphericity due to their partially elongated shape compared to the Al_2O_3 powder. The PEEK powder is of a polygonal shape and has the lowest sphericity and roundness of the powders investigated. Gravimetric sieve analyses according to ISO 4497:2020-10 [55] were performed to determine the particle size distributions (balance of type: PNJ 600-3 M; manufacturer: Kern & Sohn GmbH, Balingen-Germany and test sieves according to ISO 3310-1 in mesh sizes 20/25/32/38/45/50/56/63/71/80 µm; manufacturer: Haver & Böcker OHG, Oelde-Germany, mounted on sieve shaker AS 200 basic; manufacturer: Retsch GmbH, Haan-Germany). The mass fractions thus obtained are first approximated by a log-normal distribution. Assuming a spherical grain shape, the mass-specific distribution is then transformed into a grain number-based distribution. The transformation is relative in the density function using the proportionality of mass and volume and the relative scaling of the sphere volume over the grain radii as

$$\varphi_{mi} \cdot r_0^3 / r_i^3 = \varphi_{Ni}, \tag{25}$$

where φ_{mi} is the value of the mass-specific density function at a location i, r_0 is the reference grain radius and r_{i} is the grain radius at a location i to be transformed. The expectancy values μ_N and standard deviations σ_N thus determined

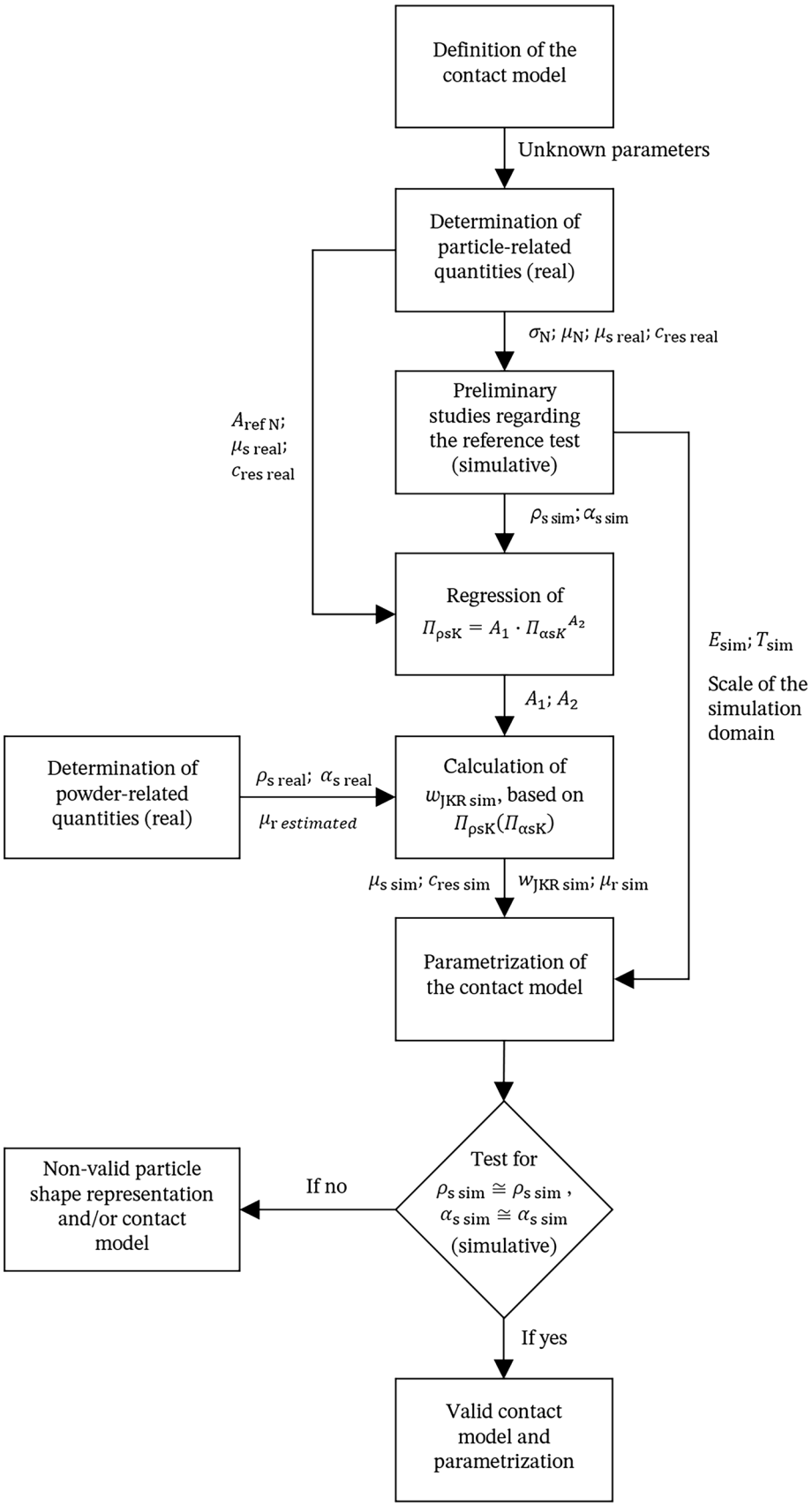

Fig. 1 Method for accelerated adaptation of model parameters for the simulation of AM powders by DEM, supported by physical size determination, a formula-based approach utilizing dimensionless quantities, while including (contact) model parameters, repose angles and bulk densities

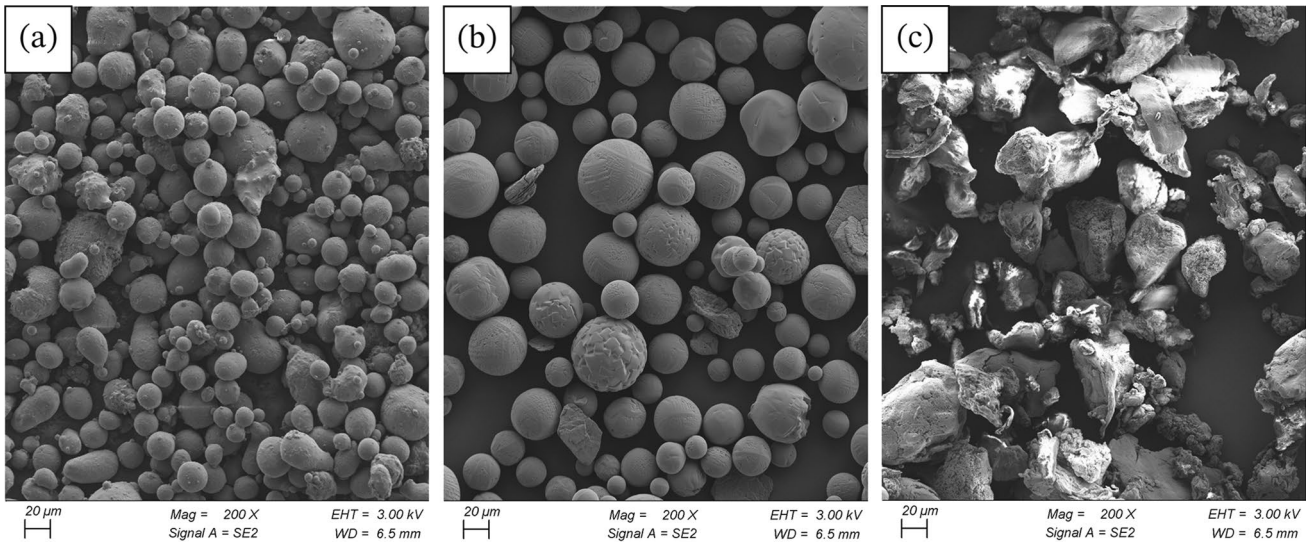

Fig. 2 SEM micrograph of the powders to be modelled; **a** AlSi10Mg powder **b** Al_2O_3 powder **c** PEEK powder

Table 1 Determined size distribution values of particle diameters for AlSi10Mg powder, Al_2O_3 powder and PEEK powder

Powder materials	Mass-specific size distribution		Number-specific size distribution	
	μ_m [µm]	σ_m [µm]	μ_N [µm]	σ_N [µm]
AlSi10Mg	35.33	1.26	33.95	1.23
Al_2O_3	46.79	1.28	42.75	1.24
PEEK	50	1.22	47.71	1.20

are given in Table 1 for distributions based both on mass and number of grains.

Determination of Sliding Friction Coefficients The physical determination of sliding friction coefficients $\mu_{s\,real}$ is carried out by inclination experiments in accordance with Nan et al. [47]. For this purpose, 20 mm · 20 mm surfaces on cuboidal sliding bodies (stereolithography part of Formlabs clear V4 with a mass of approx. 14 g) are coated with the powders, using a silane coating as an adhesion promoter. After curing (6 h at 55 °C), the coating was inspected using a confocal laser scanning microscope (LSM; type: VK-X160K; manufacturer: Keyence, Osaka-Japan). The degree of particle coverage, illustrated in Fig. 3, minimizes potential confounding influences arising from the contact between the stereolithography material and the substrate on which the sliding bodies are placed, thereby increasing the reliability of the tribological analysis.

Preliminary to each experiment, the substrate plates are cleaned with isopropanol and aerated. The angle of inclination of the substrate plates is increased with a micrometer screw until the onset of a sliding motion is observed. Afterwards, the corresponding inclination angle is measured based on a digital image. Finally, the sliding friction coefficients are determined from the tangent of the angles according to Table 2.

Determination of Restitution Coefficients The physical determination of restitution coefficients $c_{res\,real}$ for material pairings according to Table 3 is carried out by means of drop experiments and is calculated from the rebound height h_{c1} and drop height h_{c0} as

$$c_{res\,real} = \left(h_{c1}/h_{c0}\right)^{1/2}. \tag{26}$$

For the drop experiments, precision spheres (distributed by HSI-Solutions GmbH, Vienna-Austria) are dropped onto substrate plates from a height of 100 mm (corresponding to an impact velocity of approximately 1.4 m/s) and rebound heights are evaluated in digital video (240 frames/s). The measurements are performed for each material pairing for opposite pairings of static and dynamic impact partners. A further velocity-dependent determination of $c_{res\,real}$ is not performed within this research.

Determination of Angle of Repose and Bulk Density Methods for the physical determination of bulk density $\rho_{s\,real}$ and the angle of repose $\alpha_{s\,real}$ are standardized in ISO 3923-1:2018:10 [56] and ISO 4324:1983–12 [57]. However, their immediate applicability must be put into perspective regarding the simulation effort, which depends on the number of simulated particles, as well as the measurement errors, which may occur in experiments conducted in physical reality. Regarding the simulation effort, a simulation scale of < 100,000 particles is rational. As 1 mm^3 contains about 20,000 particles for the particle size distributions investigated here, the dimensions of the standardized experimental setups are required to be adapted for a limitation

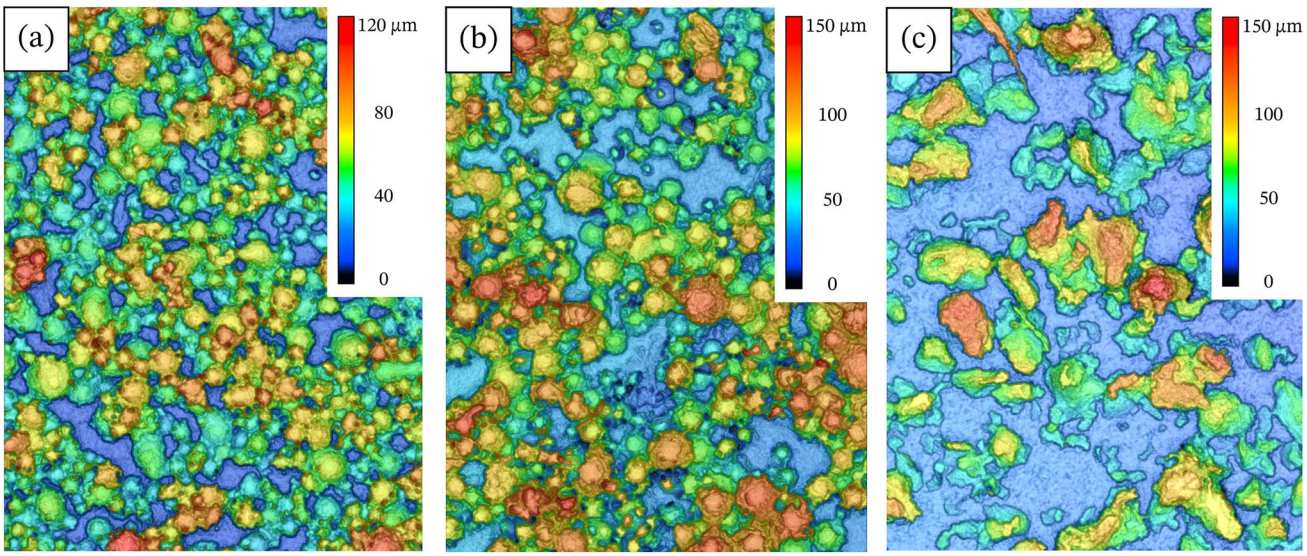

Fig. 3 LSM micrograph (height of 650 µm, width of 500 µm) of sliding blocks coated with **a** AlSi10Mg powder, **b** Al_2O_3 powder and **c** PEEK powder

Table 2 Coefficients of sliding friction $\mu_{s\ real}$, with coverage factors k and confidence levels p, determined by inclination experiments for AlSi10Mg, Al_2O_3 and PEEK and surface roughness of substrates R_z measured by LSM (square measuring area of 250 µm side length)

Coefficients of sliding friction $\mu_{s\ real}$ [–]		Substrate material		
		AlSi10Mg $R_z = 3.4$ µm	Al_2O_3 $R_z = 17.4$ µm	PEEK $R_z = 4.1$ µm
Powder materials	AlSi10Mg	0.20 ± 0.0179, $k = 2.78$, $p = 95\%$	0.45 ± 0.1493, $k = 2.78$, $p = 95\%$	0.26 ± 0.0025, $k = 2.78$, $p = 95\%$
	Al_2O_3	0.19 ± 0.0078, $k = 2.78$, $p = 95\%$	0.33 ± 0.0040, $k = 2.78$, $p = 95\%$	0.17 ± 0.0080, $k = 2.78$, $p = 95\%$
	PEEK	0.26 ± 0.0050, $k = 2.78$, $p = 95\%$		0.52 ± 0.0300, $k = 2.78$, $p = 95\%$

Table 3 Restitution coefficients $c_{res\ real}$, with coverage factors k and confidence levels p, determined by drop experiments for AlSi10Mg, Al_2O_3, PEEK substrates and spheres of comparable material

Coefficients of restitution $c_{res\ real}$ [–],drop height: 100 mm		Substrate material		
		AlSi10Mg	Al_2O_3	PEEK
Material of the sphere being dropped	Al Sphere diameter: 3.18 mm	0.54 ± 0.006 $k = 2.78$, $p = 95\%$	0.42 ± 0.010 $k = 2.78$, $p = 95\%$	0.80 ± 0.024 $k = 2.78$, $p = 95\%$
	Al_2O_3 Sphere diameter: 3.00 mm	0.54 ± 0.009 $k = 2.78$, $p = 95\%$	0.84 ± 0.024 $k = 2.78$, $p = 95\%$	0.78 ± 0.028 $k = 2.78$, $p = 95\%$
	PEEK Sphere diameter: 3.00 mm	0.97 ± 0.015 $k = 2.78$, $p = 95\%$	0.91 ± 0.006 $k = 2.78$, $p = 95\%$	0.84 ± 0.022 $k = 2.78$, $p = 95\%$

of calculation time. To avoid scaling-related disturbances between simulation and reality, an identically scaled physical setup is reasonable. However, this can only be followed to a limited extent in terms of preparation and measurement, as the relative measurement error increases with the size of the system and can significantly influence further procedures. The physical determination of the bulk density $\rho_{s\ real}$ is therefore performed using a standardized 25 cm^3 cup, while the simulatively obtained bulk density $\rho_{s\ sim}$ is determined using a scaled setup. The determination of $\alpha_{s\ real}$ is performed optically, which allows to adapt the scale of the physical experiments to the simulation scale. For this purpose, the powder is applied from an orifice diameter of 0.5 mm onto a table with a diameter of 5 mm. Finally, $\alpha_{s\ real}$ is determined by manually applying tangents (Fig. 4, values in Table 4).

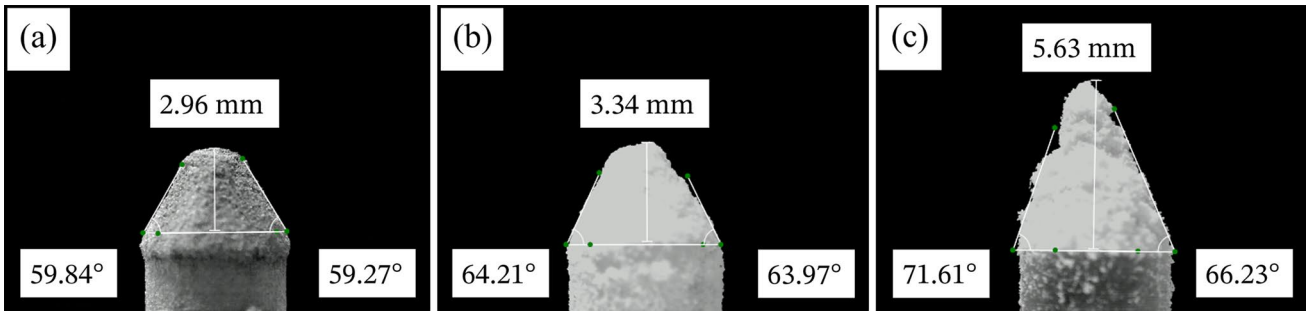

Fig. 4 Measurements of $\alpha_{s\ real}$ with manually applied tangents for **a** AlSi10Mg, **b** Al_2O_3 and **c** PEEK powder. The powder feed (orifice diameter of 500 µm) is positioned 12 mm above the deposit table (diameter of 5 mm)

Table 4 Angle of repose $\alpha_{s\ real}$ and bulk densities $\rho_{s\ real}$ with corresponding coverage factors k and confidence levels p for AlSi10Mg, Al_2O_3 and PEEK powders

	Powder material		
	AlSi10Mg	Al_2O_3	PEEK
$\alpha_{s\ real}$ [°]	60.73 ± 4.62, k = 2.26, p = 95%	61.96 ± 6.12, k = 2.26, p = 95%	70.09 ± 5.62, k = 2.26, p = 95%
$\rho_{s\ real}$ [g/cm^3]	1.33 ± 0.012, k = 2.78, p = 95%	1.95 ± 0.016, k = 2.78, p = 95%	0.29 ± 0.0035, k = 2.78, p = 95%

3.2 DEM-Models and Incorporation of Previously Determined Parameters

The simulations of bulk density and angle of repose experiments are carried out using the software EDEM (Altair Engineering Inc., Troy-USA). The contact model with mono-spherical particles previously discussed is applied in accordance with the determined particle size distribution. Deviations from the particle shapes are accounted for by adapting μ_r. The previously determined restitution coefficients can be transferred to the DEM model as averaged values of the corresponding impact pairs ($c_{res\ sim} = c_{res\ real}$). The same applies to the coefficients of friction, except for the values determined for the Al_2O_3 substrate. Due to its significantly higher surface roughness, these values must be corrected. The applied correction assumes a linear relationship between the average roughness R_z and the friction coefficient, while neglecting the linearization error in the tangent (< 5%) by comparing the results of the contact pair AlSi10Mg and Al_2O_3. The correction factor of 1/2.37 determined this way is multiplied with the measurement result for the contact pairing Al_2O_3-Al_2O_3 and the result is transferred to the DEM simulation ($\mu_{s\ sim} = \mu_{s\ real}$).

To reduce the simulation effort, the simulations are scaled down. Regarding the angle of repose, an application table with a diameter of 2 mm and an orifice with a diameter of 0.5 mm located 4 mm above the application table are used. Regarding the bulk density, the filling of a cup with a diameter of 1.95 mm and a height of 2.3 mm is simulated, which corresponds to a scaling of the 25 cm^3 standard cup to 6.5%. The simulation parameters used in the study are listed in Table 5.

4 Results and Discussion

In this chapter, the simulation results are presented and analyzed with the aim of linking relevant input variables of the virtual experiments presented. First, influences on simulation results are investigated, which result from scaling the Young's modulus applied in the simulation E_{sim} as well as the time step size T_{sim}. The aim is to minimize the computational effort and to evaluate effects of the parameter variations with respect to the quality of the simulation result. Subsequently, by analyzing the relationships between $\mu_{s\ sim}$, $\mu_{r\ sim}$, $w_{JKR\ sim}$ and the resulting quantities $\alpha_{s\ sim}$ and $\rho_{s\ sim}$, a correlation is derived using Buckingham's pi- theorem [58].

4.1 Pre-Evaluation of Scaling Effects

In chapter 3.2, reducing the Young's modulus of the contact partners and increasing the smallest grain diameter were described as options to mitigate the computational effort. The latter is excluded here because the geometries of the simulated structure and the grains have almost the same order of magnitude, which increases the risk of stochastic influences. Furthermore, a reduction of the Young's modulus E_{sim} is applicable for the considered material models. However, the influence of this measure on the simulation accuracy must be evaluated in advance. The same applies to T_{sim}. The evaluation of the influence of the variations is based on simulations of the angle of repose in one-parameter experiments. Regarding T_{sim}, the influence on the bulk density is also investigated.

Table 5 Parameters used in DEM simulations and further analyses sorted by powder types

Parameters	Symbols	Units	Values and value ranges
AlSi10Mg			
Young's modulus	E_{sim}	Pa	75×10^5–75×10^9 (equals 0.01–100% of E_{real})
Poisson's ratio	ν	[–]	0,33
Surface energy density	$w_{JKR\ sim}$	J/m^2	5×10^{-4}–3.5×10^{-3}
Solid density of a particle	ρ	kg/m^3	2670
Surface of a reference particle	A_{refN}	m^2	3.27×10^{-9}
Expected value (log-normal, N-spec.)	μ_N	m	33.95×10^{-6}
Standard deviation (log-normal, N-spec.)	σ_N	m	1.23×10^{-6}
Lower capping value ($\varphi_{Ni} \leq 3.5\%$)	c_{low}	µm	20
Upper capping value ($\varphi_{Ni} \leq 0.35\%$)	c_{high}	µm	60
Coefficient of sliding friction	$\mu_{s\ sim}$	[–]	0.2 and 0.4
Coefficient of rolling friction	$\mu_{r\ sim}$	[–]	0.02–0.12
Coefficient of restitution	$c_{res\ sim}$	[–]	0.54
Time step	T_{sim}	s	1.04×10^{-8}–1.04×10^{-6}
Al_2O_3			
Young's modulus	E_{sim}	Pa	39×10^6–39×10^{10} (equals 0.01–100% of E_{real})
Poisson's ratio	ν	[–]	0.225
Surface energy density	$w_{JKR\ sim}$	J/m^2	5×10^{-4}–2×10^{-2}
Solid density of a particle	ρ	kg/m^3	3970
Surface of a reference particle	A_{refN}	m^2	6.14×10^{-9}
Expected value (log-normal, N-spec.)	μ_N	m	42.75×10^{-6}
Standard deviation (log-normal, N-spec.)	σ_N	m	1.24×10^{-6}
Lower capping value ($\varphi_{Ni} \leq 3.5\%$)	c_{low}	µm	25
Upper capping value ($\varphi_{Ni} \leq 0.35\%$)	c_{high}	µm	80
Coefficient of sliding friction	$\mu_{s\ sim}$	[–]	0.14
Coefficient of rolling friction	$\mu_{r\ sim}$	[–]	0.014–0.14
Coefficient of restitution	$c_{res\ sim}$	[–]	0.84
Time step	T_{sim}	s	6.79×10^{-9}–6.79×10^{-7}
PEEK			
Young's modulus	E_{sim}	Pa	37×10^4–37×10^8 (equals 0.01–100% of E_{real})
Poisson's ratio	ν	[–]	0.36
Surface energy density	$w_{JKR\ sim}$	J/m^2	5×10^{-4}–4×10^{-3}
Solid density of a particle	ρ	kg/m^3	1300
Surface of a reference particle	A_{refN}	m^2	7.46×10^{-9}
Expected value (log-normal, N-spec.)	μ_N	m	47.71×10^{-6}
Standard deviation (log-normal, N-spec.)	σ_N	m	1.20×10^{-6}
Lower capping value ($\varphi_{Ni} \leq 3.5\%$)	c_{low}	µm	30
Upper capping value ($\varphi_{Ni} \leq 0.35\%$)	c_{high}	µm	80
Coefficient of sliding friction	$\mu_{s\ sim}$	[–]	0.52
Coefficient of rolling friction	$\mu_{r\ sim}$	[–]	0.26–0.52
Coefficient of restitution	$c_{res\ sim}$	[–]	0.84
Time step	T_{sim}	s	4.93×10^{-8}–4.93×10^{-6}

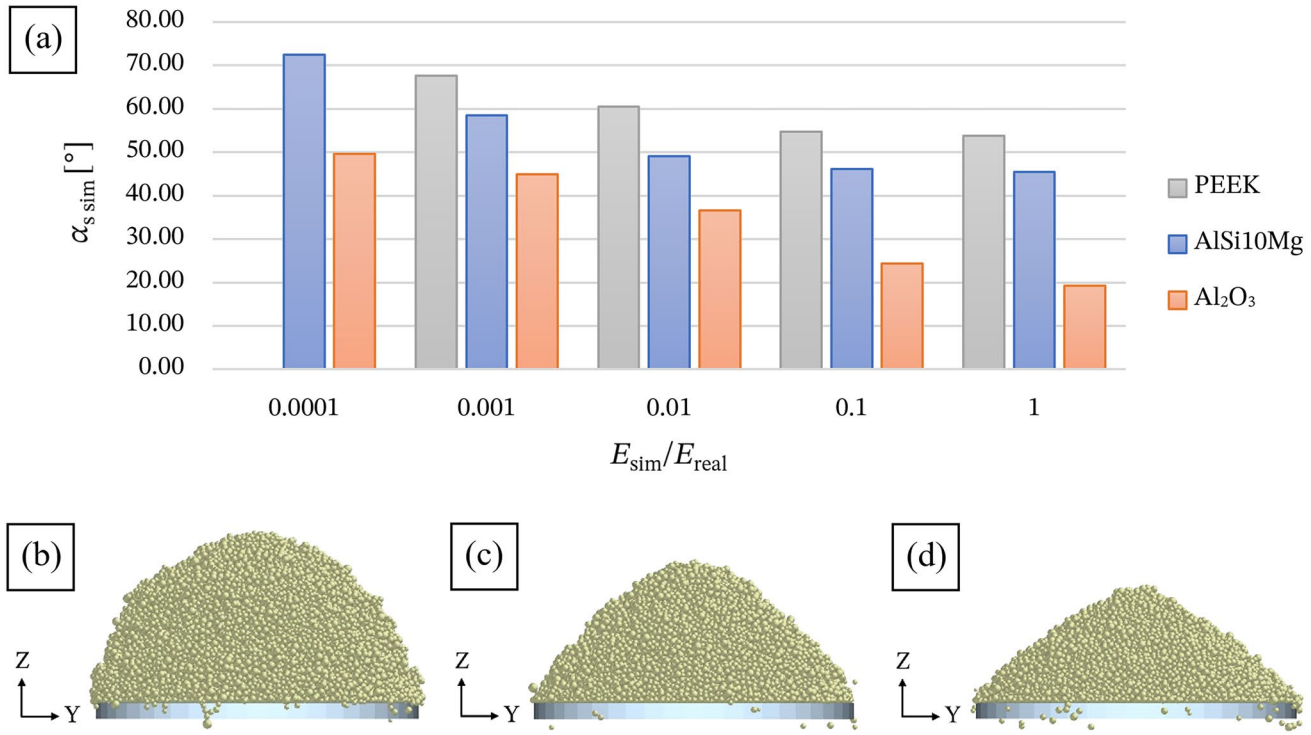

Fig. 5 **a** Influence of the ratio between the Young's modulus E_{sim} used in the simulations and the Young's modulus in physical reality E_{real} on the angle of repose for AlSi10Mg, Al_2O_3 and PEEK powders and corresponding bulk cones on circular plates of 2 mm diameter for AlSi10Mg, at **b** $E_{sim}/E_{real} = 10^{-4}$, **c** $E_{sim}/E_{real} = 10^{-3}$ and **d** $E_{sim}/E_{real} = 1$

For a better comparability of the simulation results, $w_{JKR\,sim}$ is scaled between the experimental series according to a simplified force similarity between surface forces and body forces as

$$F_{ko}/F_{tr} \rightarrow F^{ij}_{JKR\,krit}\left(r_{refN}\right)/\left(m_{refN} \cdot g\right). \tag{27}$$

Here r_{ref} describes the radius of a reference grain, according to

$$r_{ref} = \sum_i \varphi_{Ni} \cdot r_{Ni} / \sum_i \varphi_{Ni}, \tag{28}$$

where φ_{Ni} is the value of the density function of the number-based grain size distribution at location i. The calculation of the reference grain mass m_{refN} can be performed analogously. Over the series of experiments, $w_{JKR\,sim}$ as an essential input variable of F_{ko} (cf. Equation 23) is normalized with respect to the largest value (Al_2O_3: $w_{JKR\,sim} = 2\text{mJ/m}^2$, following a factorization of $2 \cdot 10^{-3}$ of Eq. 27).

Considering natural behavior of the bulk, as evaluation criterion for the determination of the scaling limit, the occurrence of a realistic bulk cone shape and less a smaller angular difference compared to the parameterization with $E_{sim} = E_{real}$ is decisive. This criterion is met for all three powders up to a reduction factor of 10^{-3} (Fig. 5).

For $E_{sim} = E_{real} \cdot 10^{-4}$, PEEK powder shows a strongly dispersive behavior, resulting in the absence of a bulk cone. Compared to AlSi10Mg and Al_2O_3, PEEK exhibits a significantly lower E_{real}. Combined with the time step criterion $T_{sim} = T_r$ used in these simulations, the associated time step difference of up to almost an order of magnitude (Fig. 6) can lead to significantly larger overlaps δ. This might promote force overshoots and dispersive behavior.

The extent to which a scaling of T_{sim} acts within constant scalings of E_{sim} is examined for the previously defined scaling limit $E_{sim} = E_{real} \cdot 10^{-3}$. All simulation results show the typical bulk cone shape in this case. At $0.2 \cdot T_r \leq T_{sim} \leq T_r$, the angle of repose differs by 6.5% for AlSi10Mg, 4.9% for PEEK, and 8.5% for Al_2O_3. Here, $\alpha_{s\,sim} \sim 1/T_r$ holds up to an approximate invariance at $T_{sim} = 0,4 \cdot T_r$ (Fig. 7), which marks the upper scaling limit. Regarding the bulk density, a similar behavior is shown with deviations from the measured values of $< 2.5\%$.

4.2 Effects of $\mu_{s\,sim}$, $\mu_{r\,sim}$ and $w_{JKR\,sim}$ and Derivation of the Pi-Diagram

To facilitate a targeted adaptation of the model parameters, the values for $\mu_{s\,sim}$, $\mu_{r\,sim}$ and $w_{JKR\,sim}$ are

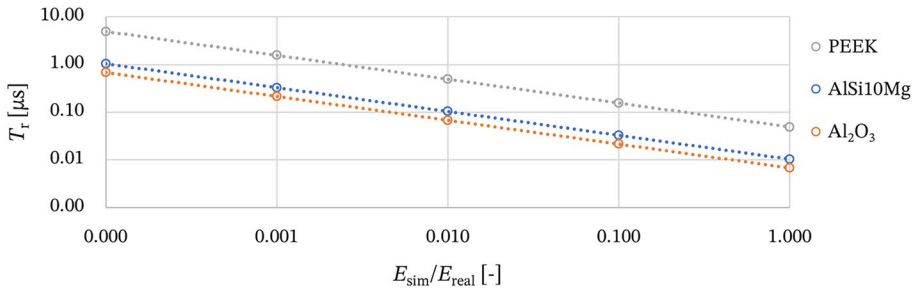

Fig. 6 Relationship between the magnitude of the Rayleigh time step T_r and the ratio between the Young's modulus E_{sim} used in the simulations and the Young's modulus in physical reality E_{real} using AlSi10Mg, Al_2O_3 and PEEK powders

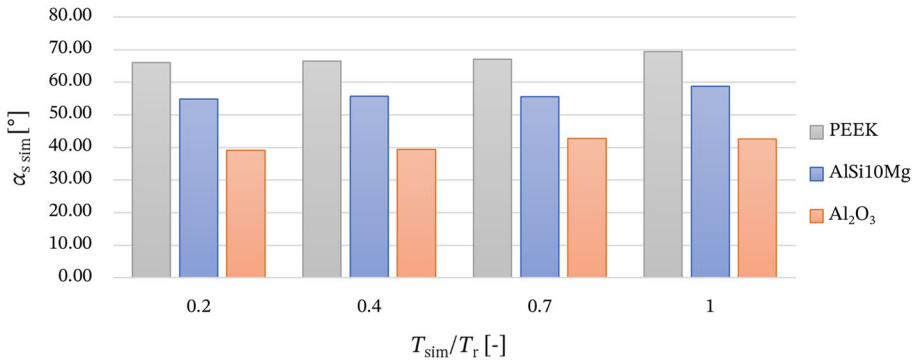

Fig. 7 Influence of the ratio between the time step size T_{sim} used in the simulations and the size of the Rayleigh time step T_r regarding the angle of repose for AlSi10Mg, Al_2O_3 and PEEK powders, at $E_{sim}/E_{real} = 10^{-3}$

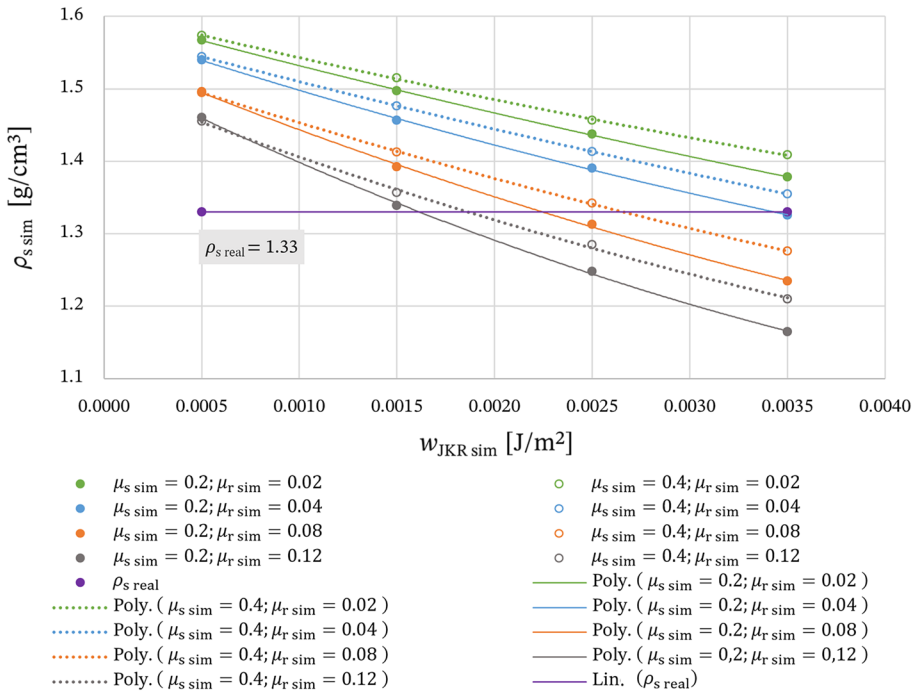

Fig. 8 Correlations between the coefficient of sliding friction $\mu_{s\,sim} = \mu_{s\,real} = 0.2$, the coefficient of rolling friction $\mu_{r\,sim}$, the surface energy density $w_{JKR\,sim}$ and the simulatively determined bulk density $\rho_{s\,sim}$ at a target density of $\rho_{s\,real} = 1.33\text{g/cm}$, using lines of constant coefficients of friction for AlSi10Mg powder

first systematically scattered around expected values, where μ_r is motivated by grain morphology [34, 35] and $w_{JKR\,sim}$ by the ranges of values commonly used in the literature [6, 9, 29–31]. In this context, the determination of material-specific lines of constant friction values for $\rho_{s\,sim}(w_{JKR\,sim})$ with $0.05 \le w_{JKR\,sim} \le 20\text{mJ/m}^2$ and $0.1 \cdot \mu_{s\,real} \le \mu_{r\,sim} \le 1.0 \cdot \mu_{s\,real}$ is first performed using the scaled bulk density experiment. For the coefficients of sliding friction and coefficients of restitution used in the simulations, the following applies: $\mu_{s\,sim} = \mu_{s\,real}$ and $c_{res\,sim} = c_{res\,real}$. The following objective functions result from $\rho_{s\,sim}(w_{JKR\,sim}) = \rho_{s\,real}$

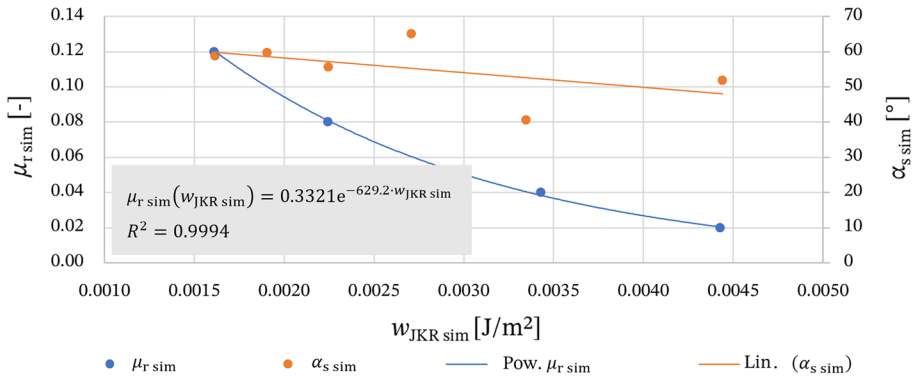

Fig. 9 Result of simulated angle of repose experiments for AlSi10Mg with parameterization derivable from Fig. 8 according to Eq. 29 (gray box)

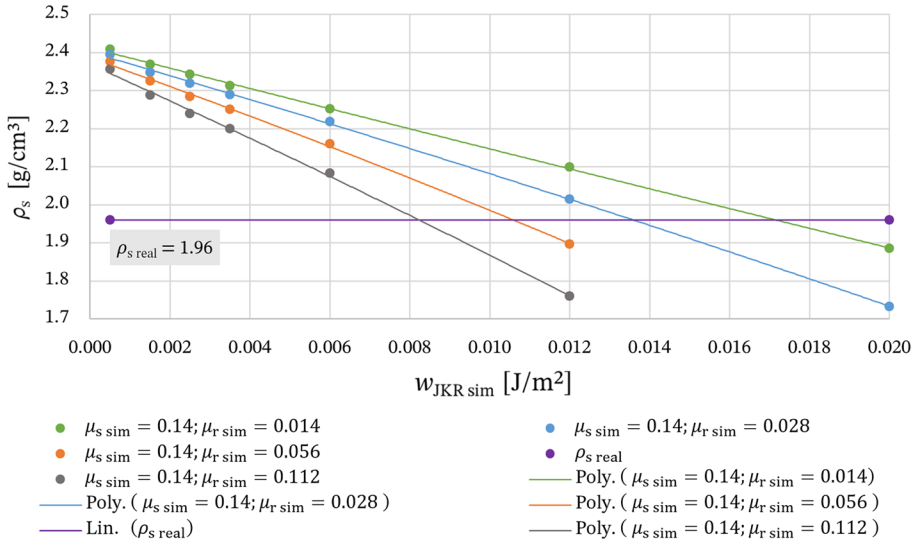

Fig. 10 Relationship between the coefficient of sliding friction $\mu_{s\,sim} = \mu_{s\,real} = 0.14$, the coefficient of rolling friction $\mu_{r\,sim}$, the surface energy density $w_{JKR\,sim}$ and the simulatively determined bulk density $\rho_{s\,sim}$ at a target density of $\rho_{s\,real} = 1.96 g/cm$, using lines of constant coefficients of friction for Al_2O_3 powder

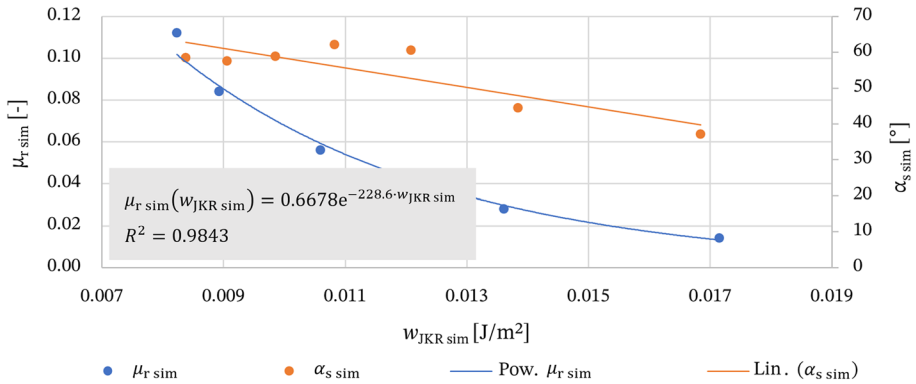

Fig. 11 Result of simulated angle of repose experiments for Al_2O_3 with parameterization derivable from Fig. 10 according to Eq. 29 (gray box)

$$\mu_{r\,sim}\left(w_{JKR\,sim}\right)\Big|\begin{matrix}\rho_{s\,sim} = \rho_{s\,real} \\ \mu_{s\,sim} = \mu_{s\,real}\end{matrix}. \tag{29}$$

These can be used to fit the model parameters with respect to $\alpha_{s\,sim} = \alpha_{s\,real}$. The simulation results obtained in this way are shown below for AlSi10Mg powder (Figs. 8 and 9) and for Al_2O_3 powder (Figs. 10 and 11). Based on the physically determined parameters, $\rho_{s\,sim}\left(w_{JKR\,sim}, \mu_{r\,sim}, \mu_{s\,sim}\right) = \rho_{s\,real}$ with $\mu_{s\,sim} = \mu_{s\,real}$ cannot be satisfied for PEEK. The lowest bulk density was determined to be 0.44 g/cm³ for $w_{JKR\,sim} = 4\ mJ/m$ and $\mu_{r\,sim} = \mu_{s\,sim}$. The compensation of significantly different grain shapes in simulation and physical reality by adjusting the coefficient of rolling friction probably reaches its limits here.

The similarity of the curves indicates a generally valid relationship between the angle of repose, the bulk density and the parameterization of the material and contact model, thus the validity of

$$\alpha_{s\,sim} = f\left(E_{sim}, \mu_{s\,sim}, \mu_{r\,sim}, c_{res\,sim}, w_{JKR\,sim}, \rho, A_{ref}, \rho_{s\,sim}\right) \tag{30}$$

can be inferred. A_{ref} describes the influence of grain size distribution, based on the surface of a reference grain, according to

$$A_{ref} = \sum_i \varphi_{Ni} \cdot A_{Ni} / \sum_i \varphi_{Ni}, \tag{31}$$

where φ_{Ni} is the value of the density function of the number-based grain size distribution at location i. The indexing of A_{Ni} is analogous. A mathematical representation of Eq. 30 can be made based on Buckingham's pi-theorem. According to its basic statement, physical relationships have validity regardless of the units used to measure the dimensions of length, mass, time and temperature. Therefore, the relationship between $\alpha_{s\,sim}$, $\rho_{s\,sim}$ and the model parameters can be described by the dimensionless parameters $\Pi_{\alpha s}$ and $\Pi_{\rho s}$. These result from a dimensional parameter analysis of Eq. 30 and solving the resulting systems of equations shown in Table 6.

Table 6 Systems of equations of dimensional analysis for (a) $\Pi_{\alpha s}$ with the nonrepeating variable α_s and (b) $\Pi_{\rho s}$ with the nonrepeating variable ρ_s

(a)	Exponent	E_{sim}	$w_{JKR\,sim} \cdot \rho$	$A_{ref} \cdot \rho$	$\tan \alpha_{s\,sim}$
	Unit of mass	1	2	1	0
	Unit of length	− 1	0	1	− 1
	Unit of time	− 2	− 5	0	0
(b)	Exponent	E_{sim}	$w_{JKR\,sim} \cdot \rho$	$A_{ref} \cdot \rho$	$\rho_{s\,sim}$
	Unit of mass	1	2	1	− 1
	Unit of length	− 1	0	1	3
	Unit of time	− 2	− 5	0	0

To obtain full rank solution vectors while including the particle density ρ, both w_{JKR} and A_{refN} are multiplied by ρ. At this point, it should be noted, that already dimensionless parameters such as $\mu_{s\,sim}$, $\mu_{r\,sim}$ and $c_{res\,sim}$ cannot be directly incorporated into

$$\Pi_{\rho s} = f\left(\Pi_{\alpha s}\right), \tag{32}$$

via dimensional analysis. Therefore, they follow as

$$\Pi_{\rho s} = E_{sim}^{-5/2} \cdot w_{JKR\,sim} \cdot \rho \cdot \left(A_{refN} \cdot \rho\right)^{-1/2} \cdot \rho_{s\,sim}, \tag{33}$$

$$\Pi_{\alpha s} = E_{sim}^{5/4} \cdot \left(w_{JKR\,sim} \cdot \rho\right)^{-1/2} \cdot \left(A_{ref} \cdot \rho\right)^{-1/4} \cdot \tan \alpha_{s\,sim}. \tag{34}$$

However, $\mu_{s\,sim}$, $\mu_{r\,sim}$ and $c_{res\,sim}$ may be included as an exponent, relativized according to their effects on $\alpha_{s\,sim}$ and $\rho_{s\,sim}$. In preliminary experiments, it was observed that an increase in c_{res} or an increase in the damping force (see Eq. 10) was observed to cause a decrease in $\alpha_{s\,sim}$ and an increase in $\rho_{s\,sim}$. The latter also occurs in the investigated area with larger ratio $\mu_{s\,sim}/\mu_{r\,sim}$ and with decreasing absolute values of the two coefficients (Figs. 8 and 10). This implies a scalability of the friction ratio by the coefficient of restitution.

Implementing K as the exponent into Eq. 32 yields

$$\Pi_{\rho sK} = f\left(\Pi_{\alpha sK}\right), \tag{35}$$

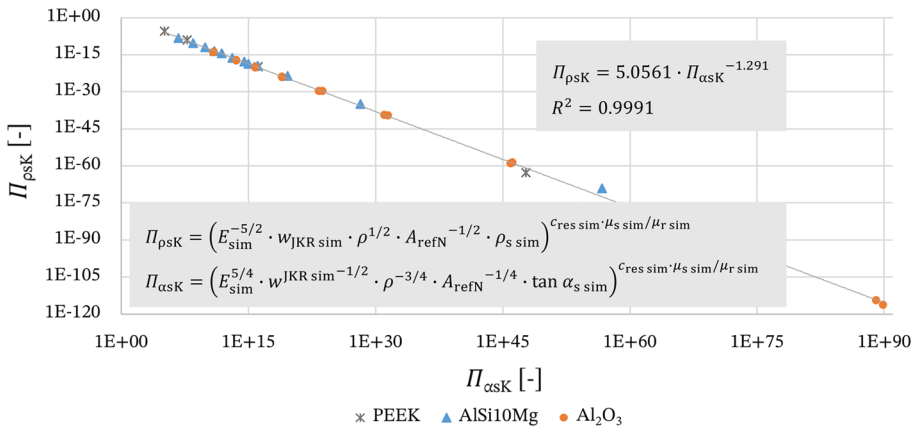

Fig. 12 Relationship between model parameters of DEM simulations, simulatively determined bulk densities and angles of repose, using a contact model with standard rolling friction model, normal and tangential force according to Hertz and Mindlin, damping forces in the same directions according to Tsuji et al., cohesive force component according to Johnson et al. as well as mono-spherical particles with logarithmically distributed grain size for AlSi10Mg, Al_2O_3 and PEEK, described with dimensionless quantities

with

$$\Pi_{\rho sK} = \Pi_{\rho s}^{K}, \tag{36}$$

$$\Pi_{\alpha sK} = \Pi_{\alpha s}^{K} \tag{37}$$

and

$$K = c_{\text{res sim}} \cdot \mu_{\text{s sim}} / \mu_{\text{r sim}}. \tag{38}$$

According to these dimensionless quantities plotted in the double logarithmic diagram, the simulatively determined experimental data can be approximated by

$$\Pi_{\rho sK} = C_1 \cdot \Pi_{\alpha sK}^{C_2}, \tag{39}$$

with $C_1 = 5.0561$ and $C_2 = -1.291$ (Fig. 12).

According to these results, the adaptation effort of the contact model parameterization can be significantly reduced with the help of the determined relationship. Therefore, the prerequisites are physically determined values of $\mu_s, c_{\text{res}}, A_{\text{ref}}$ and ρ_s, which can be obtained in already standardized or standardizable experiments with limited effort.

Since the regression performed here is based on values with, in part, significant standard deviations, it is suggested to perform regressions for the material models individually. As the regression line can already be determined with only two simulation sets for bulk density and angle of repose experiments, the necessity for a scaled down simulation domain is reduced. Thus, larger simulation domains and higher particle numbers can be used, which leads to an improved quality of the simulation results in statistical terms. Thus, an equation-based parameter adaptation can be accomplished, where w_{JKR} can be calculated for $\mu_{\text{r estimate}}$ such that $\alpha_{\text{s sim}} = \alpha_{\text{s real}}$ and $\rho_{\text{s sim}} = \rho_{\text{s real}}$ are satisfied in reasonable approximation.

5 Conclusion and Outlook

In this research, a novel method for parameter adaptation and validation in DEM based on dimensionless quantities was presented using AlSi10Mg, Al_2O_3 and PEEK powders as examples. Within this method coefficients of sliding friction, coefficients of restitution, grain size distributions and corresponding values as well as repose angles and bulk densities were determined through physical experiments. Utilizing these parameters, a regression function of two dimensionless quantities was derived, which enabled the calculation of the surface energy density necessary to adequately approximate both the previously determined angle of repose and the bulk density in simulation environment.

In this context, the present study initially focused on the analysis of physical models applicable to depict the properties of common powders used in powder bed-based additive manufacturing in DEM. One goal was to obtain corresponding relevant influential variables. Supplemented by evaluation and inclusion of common measures to reduce the specific simulation effort (reduction of Young's modulus, maximizing time step size), simulations of comprehensive parameter combinations were performed. In conjunction with a dimensional analysis of the previously determined influential variables, findings inferred from the simulation results were used to derive the two dimensionless quantities mentioned. The validity of the method was demonstrated when applied to powders with spherical grains, but limitations were noted in approximating the behavior of powders characterized by highly polygonal grain shapes.

Ultimately, the presented method facilitates a notable mitigation of the computational efforts associated with adapting DEM models of powders used in powder bed-based additive manufacturing. Moreover, it represents an integrative constituent that supports further research efforts based on DEM. The adaptation of the method to alternative reference experiments or influencing variables as well as to various contact models is conceivable and could significantly reduce the effort for simulation-based optimizations for many different kinds of powder-based processes.

Funding Open Access funding enabled and organized by Projekt DEAL.

Declarations

Conflict of interest On behalf of all authors, the corresponding author states that there is no conflict of interest associated with this script.

References

1. Vlock S, Klöden B, Kirchner A, Weißgärber T, Kieback B (2019) Powders for powder bed fusion: a review. Prog Addit Manuf 4(4):383–397. https://doi.org/10.1007/s40964-019-00078-6
2. Rehme O (2010) Cellular Design for Laser Freeform Fabrication, 1st ed. Schriftenreihe Lasertechnik, v.4. Cuvillier Verlag, Göttingen

3. (2014) VDI 3405:2014–12, Additive Fertigungsverfahren Grundlagen, Begriffe, Verfahrensbeschreibungen. Beuth Verlag GmbH, Berlin
4. Kyogoku H, Ikeshoji TT (2020) A review of metal additive manufacturing technologies: Mechanism of defects formation and simulation of melting and solidification phenomena in laser powder bed fusion process. Mech Eng Rev. https://doi.org/10.1299/mer.19-00182
5. Tan JHK, Sing SL, Yeong WY (2020) Microstructure modelling for metallic additive manufacturing: a review. Virtual Phys Prototyping 15(1):87–105. https://doi.org/10.1080/17452759.2019.1677345
6. Shaheen MY, Thornton AR, Luding S, Weinhart T (2021) The influence of material and process parameters on powder spreading in additive manufacturing. Powder Technol 383:564–583. https://doi.org/10.1016/j.powtec.2021.01.058
7. Ahmed M, Pasha M, Nan W, Ghadiri M (2020) A simple method for assessing powder spreadability for additive manufacturing. Powder Technol 367:671–679. https://doi.org/10.1016/j.powtec.2020.04.033
8. Averardi A, Cola C, Zeltmann SE, Gupta N (2020) Effect of particle size distribution on the packing of powder beds: a critical discussion relevant to additive manufacturing. Mater Today Commun. https://doi.org/10.1016/j.mtcomm.2020.100964
9. Chen H, Chen Y, Liu Y, Wei Q, Shi Y, Yan W (2020) Packing quality of powder layer during counter-rolling-type powder spreading process in additive manufacturing. Int J Mach Tools Manuf 153:10. https://doi.org/10.1016/j.ijmachtools.2020.103553
10. He Y, Gardy J, Hassanpour A, Bayly AE (2020) A digital-based approach for characterising spread powder layer in additive manufacturing. Mater Des. https://doi.org/10.1016/j.matdes.2020.109102
11. Meier C, Weissbach R, Weinberg J, Wall WA, Hart AJ (2019) Critical influences of particle size and adhesion on the powder layer uniformity in metal additive manufacturing. J Mater Process Technol 266:484–501. https://doi.org/10.1016/j.jmatprotec.2018.10.037
12. Bhalode P, Ierapetritou M (2020) Discrete element modeling for continuous powder feeding operation: calibration and system analysis. Int J Pharm. https://doi.org/10.1016/j.ijpharm.2020.119427
13. Geer S, Bernhardt-Barry ML, Garboczi EJ, Whiting J, Donmez A (2018) A more efficient method for calibrating discrete element method parameters for simulations of metallic powder used in additive manufacturing. Granular Matter 20(4):1–17. https://doi.org/10.1007/s10035-018-0848-4
14. Lampitella V, Trofa M, Astarita A, D'Avino G (2021) Discrete element method analysis of the spreading mechanism and its influence on powder bed characteristics in additive manufacturing. Micromachines (Basel). https://doi.org/10.3390/mi12040392
15. Lischka C, Nirschl H (2022) Calibration of li-ion cathode materials for discrete element method simulations. Energy Tech. https://doi.org/10.1002/ente.202200849
16. Ma Y, Evans TM, Philips N, Cunningham N (2020) Numerical simulation of the effect of fine fraction on the flowability of powders in additive manufacturing. Powder Technol 360:608–621. https://doi.org/10.1016/j.powtec.2019.10.041
17. Hertz HR (1882) Über die Berührung fester elastischer Körper und über die Härte. Verhandlung des Vereins zur Beförderung des Gewerbefleißes, Berlin, p 11
18. Johnson KL, Kendall K, Roberts AD (1971) Surface energy and the contact of elastic solids. Proc R Soc Lond A 324(1558):301–313. https://doi.org/10.1098/rspa.1971.0141
19. Mindlin RD (1949) Compliance of Elastic Bodies in Contact. J Appl Mech 16(3):259–268. https://doi.org/10.1115/1.4009973
20. Tsuji Y, Tanaka T, Ishida T (1992) Lagrangian numerical simulation of plug flow of cohesionless particles in a horizontal pipe. Powder Technol 71(3):239–250. https://doi.org/10.1016/0032-5910(92)88030-L
21. Cundall PA, Strack ODL (1979) A discrete numerical model for granular assemblies. Géotechnique 29(1):47–65. https://doi.org/10.1680/geot.1979.29.1.47
22. Castellanos A (2005) The relationship between attractive interparticle forces and bulk behaviour in dry and uncharged fine powders. Adv Phys 54(4):263–376. https://doi.org/10.1080/17461390500402657
23. Israelachvili JN (2015) Intermolecular and surface forces, 3rd edn. Elsevier Science, Saint Louis
24. Walton OR (2008) Review of adhesion fundamentals for micron-scale particles. KONA 26:129–141. https://doi.org/10.14356/kona.2008012
25. Hou X-y, Jiang J, Ding T-x, Pan W-j, Wang L, Yue H-h, Tzou H-s (2014) Experimental study of particle removal with PLZT induced voltages. In: Proceedings of the 2014 Symposium on Piezoelectricity, Acoustic Waves, and Device Applications (SPAWDA). IEEE, Piscataway, New York, pp 80–85
26. Fearing RS (1995) Survey of sticking effects for micro parts handling. In: Proceedings of the 1995 International Conference on Intelligent Robots and Systems. IEEE, Los Alamitos, California, pp 212–217
27. Soroori S, Kulinsky L, Madou M (2012) Centrifugal microfluidics: characteristics and possibilities. In: Microfluidics and microscale transport processes. CRC Press, pp 147–184
28. Böhringer KF, Donald BR Micro contacts and micro manipulation with MEMS actuator arrays
29. Jones JB (2013) Investigation of laser printing for 3D printing and additive manufacturing. Dissertation, University of Warwick
30. Sinclair CW, Edinger R, Sparling W, Molavi-Kakhki A, Labrecque C (2021) Vibratory powder feeding for powder bed additive manufacturing using water and gas atomized metal powders. Materials (Basel). https://doi.org/10.3390/ma14133548
31. Parteli EJR, Pöschel T (2016) Particle-based simulation of powder application in additive manufacturing. Powder Technol 288:96–102. https://doi.org/10.1016/j.powtec.2015.10.035
32. Johnson KL (1985) Contact mechanics. Cambridge University Press, Cambridge
33. Horabik J, Molenda M (2016) Parameters and contact models for DEM simulations of agricultural granular materials: a review. Biosys Eng 147:206–225. https://doi.org/10.1016/j.biosystemseng.2016.02.017
34. Soltanbeigi B, Podlozhnyuk A, Kloss C, Pirker S, Ooi JY, Papanicolopulos S-A (2021) Influence of various DEM shape representation methods on packing and shearing of granular assemblies. Granular Matter. https://doi.org/10.1007/s10035-020-01078-y
35. Tripathi A, Kumar V, Agarwal A, Tripathi A, Basu S, Chakrabarty A, Nag S (2021) Quantitative DEM simulation of pellet and sinter particles using rolling friction estimated from image analysis. Powder Technol 380:288–302. https://doi.org/10.1016/j.powtec.2020.11.024
36. Zhou YC, Wright BD, Yang RY, Xu BH, Yu AB (1999) Rolling friction in the dynamic simulation of sandpile formation. Phys

A 269(2–4):536–553. https://doi.org/10.1016/S0378-4371(99)00183-1
37. Brilliantov NV, Pöschel T (1998) Rolling friction of a viscous sphere on a hard plane. Europhys Lett 42(5):511–516. https://doi.org/10.1209/epl/i1998-00281-7
38. Meier C, Weissbach R, Weinberg J, Wall WA, John Hart A (2019) Modeling and characterization of cohesion in fine metal powders with a focus on additive manufacturing process simulations. Powder Technol 343:855–866. https://doi.org/10.1016/j.powtec.2018.11.072
39. Herbold E, Walton O, Homel M (2015) Simulation of powder layer deposition in additive manufacturing processes using the discrete element method. https://doi.org/10.2172/1239200
40. Luding S (2006) About contact force-laws for cohesive frictional materials in 2D and 3D. Behav Granul Media 9:137–147
41. Roessler T, Katterfeld A (2018) Scaling of the angle of repose test and its influence on the calibration of DEM parameters using upscaled particles. Powder Technol 330:58–66. https://doi.org/10.1016/j.powtec.2018.01.044
42. Kremmer M, Favier JF (2001) A method for representing boundaries in discrete element modelling-part II: kinematics. Int J Numer Meth Eng 51(12):1423–1436. https://doi.org/10.1002/nme.185
43. Kafui KD, Thornton C, Adams MJ (2002) Discrete particle-continuum fluid modelling of gas–solid fluidised beds. Chem Eng Sci 57(13):2395–2410. https://doi.org/10.1016/S0009-2509(02)00140-9
44. Li Y, Xu Y, Thornton C (2005) A comparison of discrete element simulations and experiments for 'sandpiles' composed of spherical particles. Powder Technol 160(3):219–228. https://doi.org/10.1016/j.powtec.2005.09.002
45. Thornton C, Randall CW (1988) Applications of theoretical contact mechanics to solid particle system simulation micromechanics of granular materials. In: Studies in applied mechanics, vol 20. Elsevier, pp 133–142. https://doi.org/10.1016/B978-0-444-70523-5.50023-0
46. Pekok MA, Setchi R, Ryan M, Gu H, Han Q, Gu D (2022) Al-Cu-Mg alloy powder reinforced with graphene nanoplatelets: morphology, flowability and discrete element simulation. JMMP 6(6):10. https://doi.org/10.3390/jmmp6060148
47. Nan W, Pasha M, Bonakdar T, Lopez A, Zafar U, Nadimi S, Ghadiri M (2018) Jamming during particle spreading in additive manufacturing. Powder Technol 338:253–262. https://doi.org/10.1016/j.powtec.2018.07.030
48. Han Q, Gu H, Setchi R (2019) Discrete element simulation of powder layer thickness in laser additive manufacturing. Powder Technol 352:91–102. https://doi.org/10.1016/j.powtec.2019.04.057
49. Richter C, Will F (2021) Introducing metamodel-based global calibration of material-specific simulation parameters for discrete element method. Minerals 11(8):848. https://doi.org/10.3390/min11080848
50. Cheng H, Shuku T, Thoeni K, Tempone P, Luding S, Magnanimo V (2019) An iterative Bayesian filtering framework for fast and automated calibration of DEM models. Comput Methods Appl Mech Eng 350:268–294. https://doi.org/10.1016/j.cma.2019.01.027
51. Tan P, Shen F, Tey WS, Zhou K (2021) A numerical study on the packing quality of fibre/polymer composite powder for powder bed fusion additive manufacturing. Virtual Phys Prototyping 16(1):1–18. https://doi.org/10.1080/17452759.2021.1922965
52. Cao L (2019) Study on the numerical simulation of laying powder for the selective laser melting process. Int J Adv Manuf Technol 105:2253–2269. https://doi.org/10.1007/s00170-019-04440-4
53. Xiang Z, Zhang M, Yan R, Yin Q, Zhang K (2021) Powder-spreading dynamics and packing quality improvement for laser powder bed fusion additive manufacturing. Powder Technol 389:278–291. https://doi.org/10.1016/j.powtec.2021.05.036
54. (2008) ISO/IEC GUIDE 98–3:2008. Uncertainty of measurement—Part 3: Guide to the expression of uncertainty in measurement (GUM:1995). Beuth Verlag GmbH, Berlin
55. (2020) DIN EN ISO 4497:2020–10. Metallpulver - Bestimmung der Teilchengröße durch Trockensiebung. Beuth Verlag GmbH, Berlin. https://doi.org/10.31030/3143762
56. (2018) DIN EN ISO 3923–1:2018. Metallpulver - Ermittlung der Fülldichte - Teil 1: Trichterverfahren. Beuth Verlag GmbH, Berlin. https://doi.org/10.31030/2823249
57. (1983) DIN ISO 4324:1983–12, Tenside; Pulver und Granulate; Bestimmung des Schüttwinkels. Beuth Verlag GmbH, Berlin. https://doi.org/10.31030/1341242
58. Buckingham E (1914) On physically similar systems; illustrations of the use of dimensional equations. Phys Rev 4(4):345–376. https://doi.org/10.1103/physrev.4.345